Journal of Computational Physics **171,** 479–508 (2001)
doi:10.1006/jcph.2001.6787, available online at http://www.idealibrary.com on IDEAL®

An Efficient Numerical Method for Studying Interfacial Motion in Two-Dimensional Creeping Flows

M. C. A. Kropinski[1]

Department of Mathematics and Statistics, Simon Fraser University, Burnaby, British Columbia, Canada V5A 1S6
E-mail: mkropins@cs.sfu.ca

Received April 27, 2000; revised December 19, 2000

We present new methods for computing the motion of two-dimensional closed interfaces in a slow viscous flow. The interfacial velocity is found through the solution to an integral equation whose analytic formulation is based on complex-variable theory for the biharmonic equation. The numerical methods for solving the integral equations are spectrally accurate and employ a fast multipole-based iterative solution procedure, which requires only $O(N)$ operations where N is the number of nodes in the discretization of the interface. The interface is described spectrally, and we use evolution equations that preserve equal spacing in arclength of the marker points. A small-scale decomposition is performed to extract the dominant term in the evolution of the interface, and we show that this dominant term leads to a CFL-type stability constraint. When in an equal arclength frame, this term is linear and we show that implicit time-integration schemes that are explicit in Fourier space can be formulated. We verify this analysis through several numerical examples.

Key Words: Stokes flow; fluid interfaces; integral equations; fast-multipole methods; small-scale decomposition.

1. INTRODUCTION

Numerical simulation has become one of the most important tools for investigating interfacial motion; however, computationally tracking fluid interfaces is a very expensive process. The reasons for this are clear: the governing fluid equations must be solved repeatedly in domains with highly complex boundaries and the dynamics of the interface may exhibit stiffness, particularly as regions of high curvature develop. Even with increased

[1] The work of this author was supported by NSERC grants WFA 0172672 and RGPIN 203326.

0021-9991/01 $35.00

speed and memory, current computational architecture is still limited, when not coupled with modern fast algorithms, in its ability to handle large-scale fluid interface problems with a high degree of accuracy.

In this paper, we present new methods for accurately and efficiently computing the motion of closed, two-dimensional fluid interfaces immersed in a Stokes flow. We also present a mathematical analysis of this motion. Our algorithms will be most beneficial for large-scale problems consisting of a number of these interfaces; however, to present our analysis and to fix our ideas, we study here the motion of a single, closed interface. The key elements of our methods are as follows. First, the governing fluid dynamics are described by an integral equation formulation which is solved using spectrally accurate, fast methods. Second, we use evolution equations that preserve equal arclength spacing of the marker points on the interface, thereby eliminating the need to redistribute points. Third, in order to capitalize on the ability to solve the integral equations with a high-degree of accuracy, we use a spectral mesh for the interface. Finally, in order to gain insight into the dynamics and to provide an analytic tool for understanding stability requirements, we perform a small-scale decomposition to determine the most dominant term in the evolution of the interface.

We find solutions to the Stokes equations by extending the integral equation methods developed in [13, 20] for solid particles to those which can handle the boundary conditions associated with fluid interfaces. Our starting point is the classical Sherman–Lauricella equation which has its analytic foundation in the complex variable theory for the biharmonic equation. The discretization of the integral equation is spectrally accurate and the fast multipole method [8, 12, 29] is used to compute the matrix–vector products in the iterative solution of the resulting linear system. With N points in the discretization of the boundary, our method requires only $O(N)$ operations, versus standard implementations of iterative schemes [9, 27] which require $O(N^2)$ operations or direct Gaussian elimination [34, 35] which are $O(N^3)$. Given the number of times the Stokes equations must be solved during the course of a simulation, this significant reduction in operation count becomes imperative when considering large-scale problems. The consequence of the less efficient algorithms is clear: thus-far, only modest-sized examples have been considered: Charles and Pozrikidis study the rheology of suspensions of up to 25 bubbles in [9] and van de Vorst and Mattheij appear to use a maximum of 17 in their studies of viscous sintering in [35].

It has been observed [34, 35] that the evolution of interfaces in a Stokes flow appears to become stiff as curvature increases. However, there appears to have been no formal analysis done to determine the source of this stiffness, and similarily, there does not seem to be a rigorous understanding of what are the stability constraints of the motion. We employ the ideas of Hou *et al.* presented in [18] for removing the stiffness from Hele–Shaw flows and inertial vortex sheet motion. Here, the authors performed a small-scale decomposition to determine the dominant term in the evolution of the interface. This analysis has been applied to elastic filaments in a Stokes flow in [31], but to this author's knowledge, not to fluid interfaces. We perform a small-scale decomposition and show that the dominant term is of first order, leading to a CFL-type stability constraint. By dynamically maintaining a mesh in which the nodes are distributed at equal arclength intervals, the dominant term appears linearly, and we can formulate implicit time-stepping algorithms that are explicit in Fourier space. With such a low-order stability constraint, it is questionable that large, stable step sizes will be of use when balanced against the need for accuracy, and we investigate this question numerically.

We see from the analysis of the interfacial dynamics that the motion of an interface in a Stokes flow is itself not intrinsically stiff, certainly not to the same degree as other examples of interface motion such as elastic filaments or Hele–Shaw flow. We argue, however, that the motion of marker points on the interface can become stiff if they are allowed to cluster at small spatial scales in regions of high curvature, and we demonstrate this point numerically with one particular mesh-refinement scheme. Since the cost of solving integral equations for Stokes flow can be high, many authors [27, 34, 35] refine the mesh in regions of high curvature in order to minimize the number of points needed for adequate resolution. The resulting stiffness cause Van de Vorst and Mattheij to use backward-difference formulae to avoid the prohibitively small step sizes needed by explicit time-stepping schemes. We show both analytically and numerically that this stiffness is avoided by using a method that maintains marker points at equal intervals in arclength.

In this work, the interface is described using a spectral mesh versus more typical descriptions such as cubic splines or polygonal approximations. These low-order descriptions limit the spatial accuracy in describing the interface, and when coupled with less efficient solutions to the integral equations, underresolved features on the interface may result. The use of spectral methods is not without their difficulties, however. We demonstrate that a straightforward calculation of the velocity via Fourier collocation leads to spurious growth of modes near the Nyquist frequency. Similar instabilities described in [18] are believed to be the result of aliasing errors and they are suppressed by filtering. Baker and Nachbin carefully analyze these instabilities in the context of vortex sheet motion in the presence of surface tension in [5]. They show through a linear stability analysis of the discrete equations that these instabilities arise from the velocity being inadequately resolved and show that a more careful discretization results in a stable method. We show numerically that by padding the spectrum in all of the collocation calculations, we appear to get a stable method. A more thorough stability analysis is needed in order to rigorously investigate the role of different spatial discretizations in these aliasing-type instabilities. We save this for future work.

We consider only two-dimensional problems here. While many physical effects are lost in this reduction of dimension, it has been seen that two-dimensional bubbles and drops retain enough of the qualitative features seen in three dimensions to maintain a high degree of physical relevance. There have been integral equation methods developed to study three-dimensional bubbles and drops in Stokes flow [23, 36], and clearly the increased computational complexity makes designing efficient algorithms even more critical. The complex variable methods presented here do not extend to three dimensions as primitive variable formulations do; however, the computational tools and general methodology are available in three dimensions [14, 15].

We begin, in the next section, by outlining the governing equations for fluid interfaces in a Stokes flow. We focus our attention on two cases, the first in which a closed interface (a bubble or drop) sits in an infinite expanse of fluid and the second in which the interface bounds the fluid domain. In Section 3, we briefly review the relevant complex variable theory for the biharmonic equation which leads to the formulation of the integral equations in Section 4. In Section 5, we discuss the dynamics of the interface. A small-scale decomposition of the interface is done to extract off the most dominant term in the motion, thus giving us the nature of the stability constraints. We show that in the equal arclength frame, an implicit treatment of the dominant term is easily inverted by the Fourier transform. In Section 6 we present our numerical methods, and we give several examples in Section 7.

2. THE GOVERNING EQUATIONS

We consider the motion of a two-dimensional closed fluid interface Γ in a slow viscous flow for two separate problems. In the first case (see Fig. 1a), Γ is immersed in an unbounded fluid domain D. Here, Γ represents either the boundary of a bubble (inner viscosity is zero) or a drop. In the second case (Fig. 1b), the fluid domain is bounded by Γ. This latter problem can be used as a model for the viscous sintering of glass (c.f. [34, 35]) or the coalescence of liquid drops (c.f. [10]).

We assume that the Reynolds number is small, thus the equations governing the fluid motion in D are given by the Stokes equations

$$\mu\nabla^2\mathbf{u} = \nabla p, \quad \nabla\cdot\mathbf{u} = 0, \quad \mathbf{x}\in D, \tag{1}$$

where $\mathbf{u} = (u, v, 0)$ is the velocity, p is pressure, and μ is the fluid viscosity. If Γ is the boundary of a drop, then the Stokes equations must also hold inside Γ,

$$\lambda\mu\nabla^2\mathbf{u}^d = \nabla p^d, \quad \nabla\cdot\mathbf{u}^d = 0, \tag{2}$$

where $\lambda > 0$ and the superscript d denotes variables inside the drop. The boundary conditions for an interface between two viscous fluids include continuity of velocity and a jump in normal stress proportional to the curvature. This latter condition is specified by

$$-(p - p^d)\delta_{ij}n_j + 2\mu\left(e_{ij} - \lambda e^d_{ij}\right)n_j = -\sigma\kappa n_i. \tag{3}$$

Here, e_{ij} is the rate-of-strain tensor

$$e_{ij} = \frac{1}{2}\left(\frac{\partial u_i}{\partial x_j} + \frac{\partial u_j}{\partial x_i}\right),$$

where the indices i and j take on the values 1 or 2 corresponding to the x- or y-directions, respectively, σ is the surface tension, and κ is the local curvature of Γ. If the fluid on one

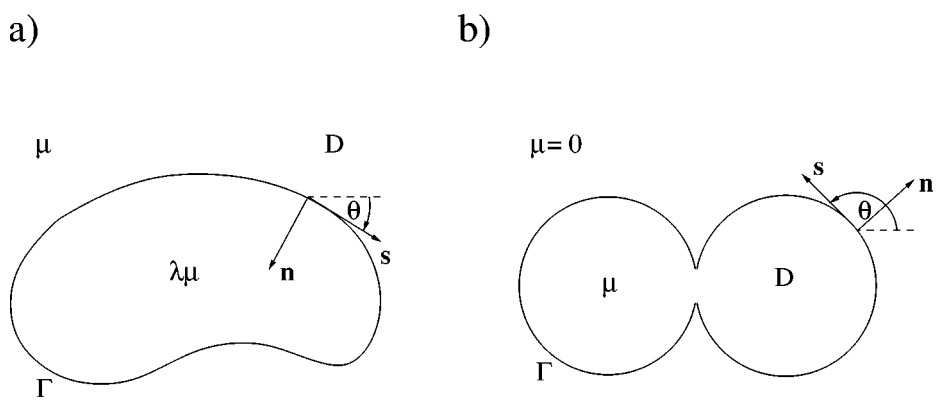

FIG. 1. A viscous fluid domain D with interface Γ: (a) a bubble or drop in an infinite expanse of fluid, (b) the fluid is bounded by Γ with an inviscid exterior. The unit normal $\mathbf{n}$ points out of D and θ is the tangent angle to Γ. The local curvature is given by $\kappa = \theta_s$, where s is arclength increasing in a clockwise direction in case (a) and counter-clockwise in case (b).

side of Γ is inviscid, then we do not require continuity of velocity, and the stress boundary condition is obtained from (3) by setting p^d and λ to be zero. If D is unbounded, then extra conditions are needed at infinity to complete the description of the problem. We have

$$\mathbf{u} \to \mathbf{u}_\infty(\mathbf{x}, t) + \frac{\dot{A}}{2\pi}\frac{\mathbf{x}}{|\mathbf{x}|^2}, \quad \text{as } |\mathbf{x}| \to \infty, \tag{4}$$

where $\mathbf{u}_\infty$ is the velocity of the incident flow and $\dot{A}$ is the prescribed rate of change of the fluid domain D (in most cases, this will be fixed at zero).

We nondimensionalize the above equations by introducing characteristic values for velocity, $u_c = \sigma/\mu$; the length of the region bounded by Γ, a; pressure, $p_c = \sigma/a$; and time, $t_c = a\mu/\sigma$. The dimensionless form of the Stokes equations are

$$\nabla^2\mathbf{u} = \nabla p, \quad \nabla \cdot \mathbf{u} = 0$$
$$\lambda\nabla^2\mathbf{u}^d = \nabla p^d, \quad \nabla \cdot \mathbf{u}^d = 0,$$

and the stress interface condition becomes

$$-(p - p^d)\delta_{ij}n_j + 2\big(e_{ij} - \lambda e^d_{ij}\big)n_j = \kappa n_i. \tag{5}$$

The motion of the interface is given by the kinematic condition which states that material points on the interface move with the velocity of the fluid. Thus, the Lagrangian description is

$$\frac{d\mathbf{x}}{dt} = \mathbf{u}(\mathbf{x}), \quad \mathbf{x} \in \Gamma.$$

Many approaches to tracking interface motion are based on the time integration of the above (c.f. [27, 34, 35], for example). However, for long-time simulations where the interface changes shape significantly, the Lagrangian description may lead to either clustering or inadequate resolution of marker points. The usual remedy is to postprocess these points in a heuristic manner to ensure proper grid spacing on the interface. Instead, we use the observation given in Hou *et al.* [18] that the shape of an interface is determined solely by its normal velocity $U = \mathbf{u} \cdot \mathbf{n}$. Consequently, a tangential component T can be introduced without changing the shape of the interface, and we choose this T to give us desirable properties in the interface dynamics [18]. The evolution equation of the interface, then, is

$$\frac{d\mathbf{x}}{dt} = U\mathbf{n} + T\mathbf{s}, \quad \mathbf{x} \in \Gamma. \tag{6}$$

We will investigate in detail a choice for T that dynamically maintains equal arclength spacing of the marker points, and we will see that this accomplishes two things. (It should be noted that others, for example [36], have added in tangential velocities as a way of controlling mesh distortion.) First, it prevents prohibitively small time steps needed by explicit methods when points cluster together. Second, it allows us to define efficient time-stepping schemes that treat the stiffest term in (6) implicitly. This will be discussed in more detail in Section 5.

3. THE BIHARMONIC EQUATION AND COMPLEX VARIABLE THEORY

For flow in two dimensions, the governing equations can be simplified by introducing a stream function $W(x, y)$ which satisfies the relations $u = W_y$, $v = -W_x$. In this way, the Stokes equations are replaced by the biharmonic equation for W,

$$\Delta^2 W(\mathbf{x}) = 0.$$

There is a complex variable theory for the biharmonic equation that has been exploited by a number of authors (c.f. [1, 6, 16, 28, 33] for example) for deriving analytical solutions for interfaces in creeping flows. This complex variable theory also provides the analytical tools for deriving the integral equations that are the basis for our numerical study. We summarize the relevant details here.

Following the discussion of Mikhlin and others [24–26], we note that any plane biharmonic function $W(x, y)$ can be expressed by Goursat's formula as

$$W(x, y) = \mathrm{Re}(\bar{z}\phi(z) + \chi(z)),$$

where ϕ and χ are analytic functions of the complex variable $z = x + iy$, and $\mathrm{Re}(f)$ denotes the real part of the complex-valued function f. The functions $\phi(z)$ and $\psi(z) = \chi'(z)$ are known as Goursat functions. All of the physical variables can be expressed in terms of these Goursat functions and they are listed here (c.f. [22]):

$$\begin{aligned} -v + iu &= \phi(z) + z\overline{\phi'(z)} + \overline{\psi(z)} \\ p &= -4\,\mathrm{Im}(\phi'), \quad p^d = -4\lambda\,\mathrm{Im}(\phi') \\ e_{11} + ie_{12} &= -e_{22} + ie_{21} = -i(z\overline{\phi''} + \overline{\psi'}). \end{aligned}$$

These expressions allow us to reduce the boundary-value problems associated with interfaces in a bounded or unbounded Stokes flow to problems in analytic function theory, namely that of finding ϕ and ψ which satisfy appropriate conditions on the boundary Γ. We outline these conditions below.

The derivation of the stress-interface condition in terms of Goursat functions closely follows that presented in [33] with slight changes in curve orientation and notation. Define $n = n_1 + in_2$, and $f = f_1 + if_2$, where $f_i = -p\,\delta_{ij}n_j + 2e_{ij}n_j$, then

$$f = 4\,\mathrm{Im}(\phi')n - 2i(z\overline{\phi''} + \overline{\psi'})\bar{n}.$$

For a point τ on the boundary Γ, the outward normal is given by $n = -i\tau_s$ (again, see Fig. 1 for orientation), which gives

$$\begin{aligned} f &= -2(\phi' - \overline{\phi'})\frac{\partial \tau}{\partial s} + 2(\tau\overline{\phi''} + \overline{\psi'})\overline{\frac{\partial \tau}{\partial s}} \\ &= -2\frac{\partial}{\partial s}(\phi - \tau\overline{\phi'} - \bar{\psi}). \end{aligned}$$

Substituting the above and $\kappa n = -\tau_{ss}$ into the interface condition (5) we get

$$\frac{\partial}{\partial s}\left\{ \lim_{z\to\tau^+}(\phi - z\overline{\phi'} - \bar{\psi}) - \lambda \lim_{z\to\tau^-}(\phi - z\overline{\phi'} - \bar{\psi})\right\} = -\frac{1}{2}\frac{\partial^2 \tau}{\partial s^2}, \quad \tau \in \Gamma$$

where τ^+ is slightly above Γ (in a direction opposite to n), and τ^- is slightly below. Integrating the above with respect to s gives

$$\lim_{z\to\tau^+}(\phi - z\overline{\phi'} - \bar{\psi}) - \lambda \lim_{z\to\tau^-}(\phi - z\overline{\phi'} - \bar{\psi}) = -\frac{1}{2}\frac{\partial \tau}{\partial s}, \quad \tau \in \Gamma. \tag{7}$$

Here, the constant of integration may be fixed to be zero. If continuity of velocity is required, then

$$\lim_{z\to\tau^+}(\phi + z\overline{\phi'} + \bar{\psi}) = \lim_{z\to\tau^-}(\phi + z\overline{\phi'} + \bar{\psi}). \tag{8}$$

If D is unbounded, then the Goursat functions must also capture the appropriate far-field velocity (4) and contain an undetermined far-field pressure term [6, 33]

$$\phi \sim -\frac{i}{4}p_\infty(t)z + \phi_\infty(z) + G(t), \quad \psi \sim \psi_\infty(z) - \bar{G}(t) - i\frac{\dot{A}}{2\pi}\frac{1}{z}, \quad \text{as } |z| \to \infty, \tag{9}$$

where $p_\infty(t)$ is determined as part of the solution, $G(t)$ is an arbitrary constant and $\phi_\infty(z)$ and $\psi_\infty(z)$ are suitably chosen analytic functions so that

$$\phi_\infty(z) + z\overline{\phi'_\infty(z)} + \overline{\psi_\infty(z)} = -i(u_\infty + iv_\infty).$$

4. THE SHERMAN–LAURICELLA INTEGRAL EQUATION

It is well known that two-dimensional Stokes flow and elasticity in the plane are closely related. Both can be expressed as biharmonic equations for a scalar potential function, although the boundary conditions may differ. An extensive theory based on complex variables has been developed for formulating integral equations for the biharmonic equation [19, 24–26, 32]. In [13], we used the classical Sherman–Lauricella equation as a starting point to formulate integral equation methods for solving a variety of boundary-value problems for Stokes flow with solid boundaries as well as isotropic elasticity in the plane. In this section, we outline the corresponding integral equations associated with fluid interfaces in a Stokes flow. (We note here that the Sherman–Lauricella integral equations can be made to be equivalent to the integral equations used in [9, 27, 34, 35], which are based on primitive variable formulations. This is discussed in detail in [13].)

We seek formulations for $\phi(z)$ and $\psi(z)$ that will be used to formulate integral equations based on satisfing the stress interface condition (7). In addition, the Goursat functions may be required to satisfy the velocity condition (8) and the far-field conditions (9). In Appendix A, we discuss the equivalence between the second fundamental problem in plane elasticity and the problem of a fluid interface bounding a viscous fluid (case b) in Fig. 1). Since representations for the Goursat functions for the former problem have been well studied, we use them for the latter, and in Section 4.1, we present the Sherman–Lauricella integral equation that results. We then present the integral equation for interfaces in unbounded domains in Section 4.2.

4.1. *Interfaces Bounding Fluid Domains*

In Appendix A, we show that we can use the representations for the Goursat functions suggested by Sherman [25, 26] for a fundamental boundary value problem for elasticity in

the plane. These representations are

$$\phi(z) = \frac{1}{2\pi i}\int_\Gamma \frac{\omega(\xi,t)}{\xi - z}\,d\xi,$$
$$\psi(z) = \frac{1}{2\pi i}\int_\Gamma \frac{-\overline{\omega(\xi,t)}\,d\xi + \omega(\xi,t)\,d\bar{\xi}}{\xi - z} - \frac{1}{2\pi i}\int_\Gamma \frac{\bar{\xi}\omega(\xi,t)}{(\xi - z)^2}\,d\xi, \tag{10}$$

where $\omega(\xi,t)$ is an unknown complex density defined on the boundary of the domain Γ. If we let z tend to a point τ on Γ and use the classical formulae for the limiting values of Cauchy-type integrals, we obtain from (7) (with $\lambda = 0$) the Sherman–Lauricella integral equation:

$$\omega(\tau,\,t) + \frac{1}{2\pi i}\int_\Gamma \omega(\xi,t)\,d\ln\frac{\xi-\tau}{\bar{\xi}-\bar{\tau}} + \frac{1}{2\pi i}\int_\Gamma \overline{\omega(\xi,t)}\,d\frac{\xi-\tau}{\bar{\xi}-\bar{\tau}} - i\frac{\bar{B}_0}{\bar{\tau}-\bar{z}_*}$$
$$= -\frac{1}{2}\frac{\partial\tau}{\partial s}. \tag{11}$$

Note that the left-hand side of the integral equation includes the term $\bar{B}_0/(\bar{\tau}-\bar{z}_*)$, where z_* is an arbitrarily prescribed point in the fluid domain D and

$$B_0 = \frac{1}{2\pi}\int_\Gamma \left[\frac{\omega(\xi,t)}{(\xi - z_*)^2}\,d\xi - \frac{\overline{\omega(\xi,t)}}{(\xi-\bar{z}_*)^2}\,d\bar{\xi}\right].$$

This term is added to ensure the invertibility of (11). Letting $\xi - \tau = re^{i\vartheta}$, a straightforward calculation shows that

$$d\ln\frac{\xi-\tau}{\bar{\xi}-\bar{\tau}} = i\,d\vartheta, \quad d\frac{\xi-\tau}{\bar{\xi}-\bar{\tau}} = 2ie^{2i\vartheta}d\vartheta.$$

Thus, (11) can be written in the form

$$\omega(\tau,t) + \frac{1}{2\pi}\int_\Gamma \omega(\xi,t)\,d\vartheta + \frac{1}{\pi}\int_\Gamma \overline{\omega(\xi,t)}e^{2i\vartheta}d\vartheta - i\frac{\bar{B}_0}{\bar{\tau}-\bar{z}_*} = -\frac{1}{2}\frac{\partial\tau}{\partial s}. \tag{12}$$

Assuming that the contours themselves are smooth, the latter form of the Sherman–Lauricella equation is clearly a Fredholm equation of the second kind with smooth kernel, and the Fredholm alternative applies. We refer the reader to [25] or [26] for a proof that (11) is invertible and that $B_0 = 0$ so long as the boundary data satisfies a compatibility condition. In the problems considered here, this compatibility condition requires that

$$\mathrm{Im}\int_\Gamma \overline{\frac{\partial\tau}{\partial s}}\,d\tau = 0,$$

which is clearly the case.

4.2. *Interfaces in Unbounded Domains*

When the fluid domain D is unbounded, we must modify the representations for ϕ and ψ to capture the far-field behaviour given by (9)

$$\phi(z) = \frac{1}{2\pi i}\int_\Gamma \frac{\omega(\xi,t)}{\xi - z}\,d\xi - \frac{i}{4}p_\infty(t)z + \phi_\infty(z) + G(t)$$

$$\psi(z) = \frac{1}{2\pi i}\int_\Gamma \frac{-\overline{\omega(\xi,t)}\,d\xi + \omega(\xi,t)\,d\bar{\xi}}{\xi - z} - \frac{1}{2\pi i}\int_\Gamma \frac{\bar{\xi}\omega(\xi,t)}{(\xi - z)^2}\,d\xi$$
$$- i\frac{\dot{A}}{2\pi}\frac{1}{z - z_c} + \psi_\infty(z) - \bar{G}(t), \tag{13}$$

where z_c is an arbitrary point inside the bubble or drop. The far-field pressure $p_\infty(t)$ is determined as part of the solution through the expression

$$p_\infty(t) = -\frac{2}{\pi}\,\mathrm{Re}\int_\Gamma \frac{\omega(\xi,t)}{(\xi - z_c)^2}\,d\xi,$$

which fixes a reference value for the pressure at z_c. Using the formulae for jumps across the interface of a Cauchy-type integral, we see that the velocity is continuous across the interface, thus (8) is satisfied automatically. Again, letting z approach a boundary point τ, we obtain from (7)

$$\omega(\tau,t) + \frac{\beta}{2\pi i}\int_\Gamma \omega(\xi,t)\,d\ln\frac{\xi - \tau}{\bar{\xi} - \bar{\tau}} + \frac{\beta}{2\pi i}\int_\Gamma \overline{\omega(\xi,t)}\,d\frac{\xi - \tau}{\bar{\xi} - \bar{\tau}} + 2\beta G(t) - i\frac{\beta}{2}p_\infty(t)\tau$$
$$= -\frac{\gamma}{2}\frac{\partial\tau}{\partial s} - \beta(\phi_\infty(\tau) - \tau\overline{\phi'_\infty(\tau)} - \overline{\psi_\infty(\tau)}), \tag{14}$$

where $\beta = (1-\lambda)/(1+\lambda)$, $\gamma = 1/(1+\lambda)$, and G is given by

$$G(t) = \frac{1}{2}\int_\Gamma \omega(\xi,t)\,ds.$$

It has been noted by other authors [17] that integral equation formulations in primitive variables can become singular in the limits $\lambda = 0$ and $\lambda = \infty$ (the drops become air bubbles or solid particles, respectively). Deflated integral equations must be formulated in order to compute solutions when λ is close to either of these two limits. In the integral equation formulation (14), $\lambda = 0$ is not a singular case. The numerical results in Example 4, Section 7 support this, and again, we refer the reader to [25] or [26] for discussions on invertibility.

When $\lambda = 1$, i.e., the drop viscosity is the same as the ambient fluid, the solution to (14) is trivial,

$$\omega = -\frac{1}{4}\frac{\partial\tau}{\partial s}, \quad \text{for } \tau \in \Gamma. \tag{15}$$

This explicit solution to (14) is a significant simplification, it has been noted by others [6, 9, 10], and it will provide a convenient test case for our numerical methods for the evolution of the drop interface.

5. DYNAMICS OF THE INTERFACE

In this section we discuss Eq. (6) for the evolution of the interface Γ. As discussed in Section 2, the shape of the evolving interface is determined solely by the normal component of the fluid velocity U on Γ, where $U = \mathrm{Re}\{(u + iv)\bar{n}\}$ and

$$\begin{aligned} u + iv &= -i \lim_{z \to \tau} (\phi + z\overline{\phi'} + \bar{\psi}), \quad \tau \in \Gamma \\ &= -\frac{1}{2\pi} \oint_\Gamma \omega(\xi, t) \left\{ \frac{d\xi}{\xi - \tau} + \frac{d\bar{\xi}}{\bar{\xi} - \bar{\tau}} \right\} + \frac{1}{2\pi} \oint_\Gamma \overline{\omega(\xi, t)}\, d\left(\frac{\xi - \tau}{\bar{\xi} - \bar{\tau}} \right) + u_\infty + iv_\infty. \end{aligned} \tag{16}$$

In the above, $\omega(\tau, t)$ is found from the solution to (11) or (14) and $\oint$ denotes a principal value integral. (It is understood that $u_\infty + iv_\infty \equiv 0$ for flows in bounded domains.) The role of the tangential velocity T in (6) is to effect a change in the frame for the parametrization of Γ. In Section 5.1, we derive an expression for T which dynamically maintains equal arclength spacing of the marker points. This is called the Equal Arclength Frame. For comparison, we give an expression for T which dynamically clusters marker points in the vicinity of regions of high curvature (called the Complexity Measuring Frame). In Section 5.2, we apply a small-scale decomposition of $u + iv$ to extract the most dominant term from the dynamics of the interface. By choosing T according to the equal arclength frame, this dominant, highest-order term appears linearly and its implicit time integration can be handled trivially by the Fourier transform.

5.1. *Curve Motion*

We introduce a parametrization of Γ so that the interface is described by $\tau = x(\alpha, t) + iy(\alpha, t)$, where $\alpha \in [0, 2\pi]$. (Note: As shown in Fig. 1, the parametrization traverses Γ counter-clockwise if Γ bounds D, and clockwise if D is unbounded.) The outward unit normal on Γ is

$$n = -i \frac{\tau_\alpha}{s_\alpha} \equiv -ie^{i\theta}.$$

Here, s is arclength, $s_\alpha = |\tau_\alpha|$, and θ is the tangent angle to Γ. We rewrite (6) as

$$\frac{d\tau}{dt} = -Ui \frac{\tau_\alpha}{s_\alpha} + T \frac{\tau_\alpha}{s_\alpha} \equiv -Uie^{i\theta} + Te^{i\theta}. \tag{17}$$

Alternatively, we could use θ and s_α as the dynamic variables, which is the approach taken in [18, 31]. In these works, a small-scale decomposition on the equation for θ_t shows the highest-order term appearing linearly in θ. As we will see in Section 5.2, a similar analysis on (17) shows that the stiffest term can be made linear in τ, thus we retain the physical coordinates as our dynamic variables. It is, however, illustrative to rewrite the evolution in terms of θ and s_α as it will aid us in deriving an expression for T that will maintain an equal arclength frame in the parametrization.

The following derivation is similar to that presented in Hou *et al.* [18], and we include it here for completeness and to incorporate our change in curve orientation. First, differentiating $\tau_\alpha = s_\alpha e^{i\theta}$ with respect to t gives

$$\frac{d\tau_\alpha}{dt} = s_{\alpha t} e^{i\theta} + s_\alpha \theta_{\alpha t} ie^{i\theta}.$$

The derivative of (17) with respect to α is

$$\frac{d\tau_\alpha}{dt} = (U\theta_\alpha + T_\alpha)e^{i\theta} + (\theta_\alpha T - U_\alpha)ie^{i\theta}.$$

Equating the right-hand sides of the above two equations gives the evolution for s_α and θ:

$$s_{\alpha t} = U\theta_\alpha + T_\alpha, \quad \theta_t = \frac{1}{s_\alpha}(\theta_\alpha T - U_\alpha). \tag{18}$$

We will see in the following section that requiring s_α to be everywhere equal to its mean will result in the most dominant term appearing linearly in the evolution equation and will prevent prohibitive stability constraints for explicit time-stepping methods. This equal arclength frame is enforced by a particular choice of T. We require

$$s_\alpha(\alpha, t) = \frac{1}{2\pi}\int_0^{2\pi} s_\alpha(\alpha', t)\, d\alpha' = \frac{1}{2\pi}L(t), \tag{19}$$

where $L(t)$ is the length of the interface Γ. By differentiating (19) with respect to t and using (18), T is found to be

$$T(\alpha, t) = T(0, t) - \int_0^\alpha \theta_{\alpha'} U\, d\alpha' + \frac{\alpha}{2\pi}\int_0^{2\pi} \theta_{\alpha'} U d\alpha'. \tag{20}$$

If s_α satisfies (19) initially, the above choice for T maintains this constraint in time.

It is possible to define a tangential velocity that can be used to dynamically refine the mesh at regions of high curvature. The Complexity Measuring Frame is achieved by ensuring that $s_\alpha(\alpha, t)C(\kappa)$ is everywhere equal to its mean, where $C(\kappa)$ is a strictly positive, smooth, increasing function of $|\kappa|$ ($C(\kappa) = 1 + \kappa^2$, for example). Thus, we wish to ensure

$$s_\alpha(\alpha, t)C(\kappa) = \frac{1}{2\pi}\int_0^{2\pi} s_{\alpha'} C(\kappa(\alpha'))\, d\alpha'$$

is maintained for all time and the choice of T that achieves this is

$$\begin{aligned} T(\alpha, t) = \frac{C|_{\alpha=0}}{C}T(0, t) - \frac{1}{C}\int_0^\alpha \left\{ \frac{dC}{d\kappa}\left(\frac{U_{\alpha'}}{s_{\alpha'}}\right)_{\alpha'} + \theta_{\alpha'} U\left(\kappa\frac{dC}{d\kappa} - C\right)\right\} d\alpha' \\ + \frac{\alpha}{2\pi C}\int_0^{2\pi} \left\{ \frac{dC}{d\kappa}\left(\frac{U_{\alpha'}}{s_{\alpha'}}\right)_{\alpha'} + \theta_{\alpha'} U\left(\kappa\frac{dC}{d\kappa} - C\right)\right\} d\alpha'. \end{aligned} \tag{21}$$

This frame was mentioned in Appendix 2 of [18] and we use it to explore the implications on stability of allowing grid points to cluster in regions of high curvature.

5.2. *Small-Scale Decomposition*

It has been observed [34, 35] that the evolution of interfaces in a Stokes flow appears to become stiff as curvature increases. As argued in [18], the stability constraints arise from the influence of high-order terms only at small spatial scales. Below we present an asymptotic analysis of the fluid velocity to determine the dominant term at small scales. We show that

if we are in the equal arclength frame, this dominant term appears linearly in the evolution equation and can be treated implicitly in a straighforward manner.

Recall from the discussion in Section 4.1 that we can rewrite the kernel in the second principal-value integral in (16),

$$\frac{1}{2\pi}\oint_\Gamma \overline{\omega(\xi,t)}\,d\left(\frac{\xi-\tau}{\bar{\xi}-\bar{\tau}}\right)=\frac{i}{\pi}\oint_\Gamma \overline{\omega(\vartheta,t)}e^{2i\vartheta}\,d\vartheta.$$

The fluid velocity on Γ then becomes

$$u+iv=-\frac{1}{2\pi}\oint_\Gamma \omega(\xi,t)\left\{\frac{d\xi}{\xi-\tau}+\frac{d\bar{\xi}}{\bar{\xi}-\bar{\tau}}\right\}+\frac{i}{\pi}\oint_\Gamma \overline{\omega(\vartheta,t)}e^{2i\vartheta}\,d\vartheta+u_\infty+iv_\infty.$$

The second integral term on the right-hand side of the above equation contains a smooth kernel and thus is a smoothing operator[2] on ω. We use the notation $f\sim g$ introduced in [18] to mean that the difference between f and g is smoother than f and g. Thus,

$$u+iv\sim-\frac{1}{2\pi}\oint_\Gamma \omega(\alpha',t)\left\{\frac{\xi_{\alpha'}}{\xi-\tau}+\frac{\bar{\xi}_{\alpha'}}{\bar{\xi}-\bar{\tau}}\right\}d\alpha'. \tag{22}$$

The Cauchy kernels in (22) can be rewritten as

$$\frac{\xi_{\alpha'}}{\xi(\alpha',t)-\tau(\alpha,t)}=\frac{1}{2}\cot\left(\frac{\alpha'-\alpha}{2}\right)+\left[-\frac{1}{2}\cot\left(\frac{\alpha'-\alpha}{2}\right)+\frac{\xi_{\alpha'}}{\xi(\alpha',t)-\tau(\alpha,t)}\right], \tag{23}$$

where the bracketed term has a removable singularity provided that τ is a smooth function of α and the interface does not self intersect. Therefore, (22) can be rewritten as

$$\begin{aligned}u+iv&\sim-\frac{1}{2\pi}\oint_\Gamma \omega(\alpha',t)\cot\left(\frac{\alpha'-\alpha}{2}\right)d\alpha'\\&=\mathcal{H}[\omega](\alpha,t),\end{aligned}$$

where $\mathcal{H}$ is the Hilbert transform [7], which is diagonalizable by the Fourier transform

$$\mathcal{H}[e^{inx}]=-i\,\mathrm{sgn}(n)e^{inx},\quad \mathcal{H}[1]=0.$$

Since ω is the solution to a Fredholm integral equation of the second kind with smooth kernel, we can use the results in Appendix 1 of [18] directly to obtain an explicit expression for ω at small scales. The dominant term of ω at small scales is given by the highest-order term on the right-hand side of the integral equations (11) or (14),

$$\omega\sim-\frac{\gamma}{2}\frac{\tau_\alpha}{s_\alpha}.$$

Denote the small-scale velocity by u^s+iv^s where

$$u^s+iv^s=-\frac{\gamma}{2}\mathcal{H}\left[\frac{\tau_\alpha}{s_\alpha}\right].$$

[2] E is a smoothing operator on ω if its Fourier transform satisfies $\hat{E}[\omega]=O(e^{-\rho|k|}\hat{\omega})$, $\rho>0$ for large wave number $|k|$. Here ρ defines the strip of analyticity given by $|\mathrm{Im}\alpha|\le\rho$.

This, then, is the most dominant term in the velocity on the interface. (We have assumed in the scaling of the variables, that surface tension is nonzero. In the case of zero surface tension, the highest-order term on the right-hand side of the integral equation is found from the ambient flow velocity. The small-scale velocity, then, would be the Hilbert transform of this term.)

If we have chosen T according to (20), then s_α is spatially invariant at fixed time and

$$u^s + iv^s = -\frac{\gamma}{2}\frac{1}{s_\alpha}\mathcal{H}[\tau_\alpha].$$

By extracting off the dominant behavior at small scales, the evolution equation (17) becomes

$$\frac{d\tau}{dt} = -\frac{\gamma}{2}\frac{1}{s_\alpha(t)}\mathcal{H}[\tau_\alpha] - i(U - U^s)\frac{\tau_\alpha}{s_\alpha(t)} + (T - T^s)\frac{\tau_\alpha}{s_\alpha(t)} \tag{24}$$

$$= -\frac{\gamma}{2}\frac{1}{s_\alpha(t)}\mathcal{H}[\tau_\alpha] + R(\alpha, t), \tag{25}$$

where U^s and T^s are the normal and tangential components of $u^s + iv^s$, respectively, and R is given by the remaining terms on the right-hand side of (24), not including the first term. Applying a Fourier transform to (25) gives

$$\frac{d\hat{\tau}}{dt}(n, t) = -\frac{\gamma}{2}|n|\frac{\hat{\tau}(n, t)}{s_\alpha(t)} + \hat{R}(n, t). \tag{26}$$

Thus, a time-integration method that treats the dominant term implicitly can be trivially inverted by the Fourier Transform. We anticipate from (26) that if τ is represented by a truncated Fourier series, a stable step size for an explicit method will be $O(1/N)$ where $N/2$ is the Nyquist frequency. Thus, the stability criteria is on the same order as a CFL constraint and we will verify this numerically. From this analysis, we can also speculate that allowing marker points to cluster, whereby s_α becomes very small in some regions, will have an adverse effect on stability. The stability constraints for the fluid interface problems in [18, 31] are of a much higher order and being able to efficiently treat the dominant term implicitly has a clear advantage. In this case, it is questionable whether being able to take large stable step sizes will balance against the need for accuracy. We will investigate this question numerically in Section 7.

6. NUMERICAL METHODS

6.1. *Spectral Description of the Interface and Time Integration Schemes*

We obtain an initial equal arclength distribution of marker points on Γ by the methods outlined in [18]. We assume we are given N even points on Γ in some convenient parametrization, where N is large enough to fully resolve the interface (i.e., the Fourier spectrum has decayed to round-off). The initialization procedure involves solving a sequence of nonlinear equations for the N marker points at equal arclength intervals using Newton's method and Fourier interpolation. Then, τ is uniformly discretized in α, where $h = 2\pi/N$ is the mesh spacing.

We use two different time-discretizations schemes to evolve $\tau(\alpha, t)$. The first applies the explicit midpoint Runge–Kutta method to (17) directly. This explicit, second-order

method is a standard approach and details can be found in [3]. Alternatively, we use an implicit-explicit method on (26). A wide variety of implicit-explicit (IMEX) multistep methods are examined in detail in [2] and from this work, we select the SBDF (semi-implicit backward differentiation formula) scheme. The SBDF scheme is also second-order and was selected over other second-order IMEX schemes because it appears, after some numerical experimentation, to have better stability properties for the problems considered here. Let Δt be the time step size and $\hat{\tau}^k$ denote the approximate solution at $t = k\Delta t$. Then the SBDF scheme applied to (26) gives

$$\frac{1}{2\Delta t}\left[3\hat{\tau}_n^{k+1} - 4\hat{\tau}_n^k + \hat{\tau}_n^{k-1}\right] = -\frac{\gamma}{2}|n|\frac{\hat{\tau}_n^{k+1}}{s_\alpha^{k+1}} + 2\hat{R}_n^k - \hat{R}_n^{k-1}. \tag{27}$$

The differential arclength is updated explicitly according to (18) using the second-order Adams–Bashforth method,

$$s_\alpha^{k+1} = s_\alpha^k + \frac{\Delta t}{2}(3M^k - M^{k-1})$$

where M is given by

$$M = \frac{1}{2\pi}\int_0^{2\pi} \theta_\alpha U \, d\alpha.$$

Multistep IMEX schemes are a more natural choice for (26) since s_α^{k+1} must be updated first. We note here that IMEX Runge–Kutta schemes have been developed [4]. These would have the advantage of being self-starting and possibly have higher accuracy.

The right-hand side of evolution equations (17) and (26) is calculated spectrally: All differentiation in α is done using the fast Fourier transform, and a spectrally accurate discretization of (16) is discussed in the following section. In a straightforward pseudospectral calculation, we compute the velocity at the N spatial nodes; however, we see growth of modes near the Nyquist frequency, particularly if the initial profile is significantly deformed. Similar instabilities described in [18] are believed to be the result of aliasing errors, and they are suppressed using a high-order Krasny filter. In [5], Baker and Nachbin carefuly analyze these instabilities in the context of vortex sheet motion in the presence of surface tension. They show through a linear stability analysis of the discrete equations that these instabilities arise from the velocity being inadequately resolved and show that a spectrally-accurate "midpoint" discretization of the velocity results in a stable method. The approach we take is to calculate the velocity at twice the number of nodes in physical space and then truncate the spectrum to the original size. This, effectively, pads the spectrum in all of the spectral calculations, and we demonstrate numerically in Section 7 that this appears to give to a stable method. It is possible that this padding procedure plays an analogous role to the midpoint discretization in [5]. However, a more thorough stability analysis is needed in order to investigate the role of different spatial discretizations in these aliasing-type instabilities. This is future work.

The Fourier spectrum is checked during the course of simulation and if the modes near the Nyquist frequency rise above round off, N is doubled. If an explicit method is being used, we select a new stable step size and according to (26) this should be

$$\Delta t^{k+1} = \frac{1}{2}\frac{s_\alpha^{k+1}}{s_\alpha^k}\Delta t^k.$$

Similarly, if the evolving shape is becoming less complex, N is halved once sufficient modes have decayed to round off and a new time step is determined by

$$\Delta t^{k+1} = 2\frac{s_\alpha^{k+1}}{s_\alpha^k}\Delta t^k.$$

6.2. *Discretization of the Integral Equation*

In order to solve the Sherman–Lauricella equations, we use a Nyström discretization based on the trapezoidal rule since it achieves super-algebraic convergence for smooth data on smooth boundaries. For this, we assume that we are given N' points on the contour Γ, equispaced with respect to the parameter α. The step length in the discretization is defined by $h = 2\pi/N'$. Here, $N' = 2N$ where N is the number of marker points on Γ and Fourier interpolation is used to get data at twice the number of nodes. Associated with each such point, denoted by τ_j, is an unknown value ω_j. The derivative τ_α will be denoted by σ and the derivative values σ_j at the discretization points are calculated via FFTs.

Consider now the system (11). After discretization, we have

$$\omega_j + \sum_{i=1}^{N'} K_1(\tau_j, \tau_i)\omega_i + \sum_{i=1}^{N'} K_2(\tau_j, \tau_i)\overline{\omega_i} = -\frac{\sigma_j}{2|\sigma_j|}. \tag{28}$$

The kernels K_1 and K_2 are given by

$$K_1(\tau_j, \tau_i) = \frac{h}{2\pi i}\left(\frac{\sigma_i}{\tau_i - \tau_j} - \frac{\overline{\sigma_i}}{\overline{\tau_i} - \overline{\tau_j}}\right)$$

$$K_2(\tau_j, \tau_i) = \frac{h}{2\pi i}\left(\frac{\sigma_i}{\overline{\tau_i - \tau_j}} - \frac{\overline{\sigma_i}(\tau_i - \tau_j)}{(\overline{\tau_i} - \overline{\tau_j})^2}\right).$$

When $\tau_j = \tau_i$, K_1 and K_2 should be replaced by the appropriate limits

$$K_1(\tau_j, \tau_j) = \frac{h}{2\pi}\kappa_j|\sigma_j|$$

$$K_2(\tau_j, \tau_j) = \frac{h}{2\pi}\kappa_j(\sigma_j)^2/|\sigma_j|,$$

where κ_j denotes the curvature at the point τ_j, calculated spectrally.

Remark. We have omitted the term B_0 in (11) since its absence does not affect the behavior of the iterative solution procedure we will employ. For a detailed discussion of this point, see [11].

The discretization of the Sherman–Lauricella equation (14) for bubbles or drops in an unbounded domain is

$$\omega_j + \beta\sum_{i=1}^{N'} K_1(\tau_j, \tau_i)\omega_i + \beta\sum_{i=1}^{N'} K_2(\tau_j, \tau_i)\overline{\omega_i} + \beta h\sum_{i=1}^{N'} \omega_i|\sigma_i|$$
$$+ i\beta\frac{h}{2\pi}\tau_j\sum_{i=1}^{N'} \mathrm{Re}\left(\frac{\omega_i\sigma_i}{(\tau_i - z_c)^2}\right) = g_j, \tag{29}$$

where

$$g_j = -\frac{\gamma}{2}\frac{\sigma_j}{|\sigma_j|} - \beta(\phi_\infty(\tau_j) - \tau_j\overline{\phi'_\infty(\tau_j)} - \overline{\psi_\infty(\tau_j)}).$$

In our implementation, the linear equations (28) and (29) are solved iteratively, using the generalized minimum residual method GMRES [30]. As discussed in detail in [13], the bulk of the work at each iteration lies in applying the full matrix to a vector, i.e., computing the product represented by the left-hand side of (28) and (29). This product can be computed in $O(N)$ time using the adaptive fast multipole method (FMM). The implementation used here was developed in [13] for problems in Stokes flow with solid boundaries and elasticity in the plane. For further details, we also refer the reader to the original papers [8, 12, 29]. Since the number of iterations needed to solve a Fredholm equation of the second kind to a fixed precision is bounded independent of the system size N, we can estimate the total cost by

$$c(\epsilon)\, C(\epsilon) N,$$

where $c(\epsilon)$ is the number of GMRES iterations needed to reduce the residual error to ϵ and $C(\epsilon)$ is the constant of proportionality in the FMM.

Once the solution ω_j has been computed, we calculate the velocity at the grid points through discretizing (16),

$$u_j + i v_j = -\frac{h}{\pi}(\omega_\alpha)_j + \sum_{i=1}^{N'} K_1'(\tau_j, \tau_i)\omega_i + i \sum_{i=1}^{N'} K_2(\tau_j, \tau_i)\overline{\omega_n} + (u_\infty + i v_\infty)_j, \quad (30)$$

where K_2 is defined previously and K_1' is

$$K_1'(\tau_j, \tau_i) = -\frac{h}{2\pi}\left(\frac{\sigma_i}{\tau_i - \tau_j} + \frac{\overline{\sigma_i}}{\overline{\tau_i} - \overline{\tau_j}}\right)$$
$$K_1'(\tau_j, \tau_j) = -\frac{h}{2\pi}\,\mathrm{Re}\left\{\frac{(\sigma_\alpha)_j}{\sigma_j}\right\}.$$

This quadrature rule is spectrally accurate and is based on subtracting off the singularity [5]. Again, FMM is used to evaluate (30). We note that in the primitive variable formulation, the integral equation is formulated in terms of the velocity, and thus an extra evaluation is not required after the integral equation has been solved. The evaluation of (30) in our formulation is equivalent to one extra GMRES iteration and is not a significant cost.

7. NUMERICAL RESULTS

The algorithms described above have been implemented in Fortran. Here, we illustrate their performance on a variety of examples. The convergence tolerance for the GMRES iteration is set to 10^{-10} and all timings cited are for a Compaq Alpha ES40.

EXAMPLE 1: NUMERICAL STABILITY. As discussed in Section 6.1, a pseudospectral calculation of the velocity (30) with $N' = N$ leads to spurious growth of the modes near the Nyquist frequency (see Fig. 2). This spurious behavior does not appear when the spectrum is padded (the velocity is evaluated first at twice the number of marker points ($N' = 2N$) and the Fourier series for the right-hand side of (17) or (26) is truncated to the original number of modes). We save, for future consideration, a more rigorous linear stability analysis of

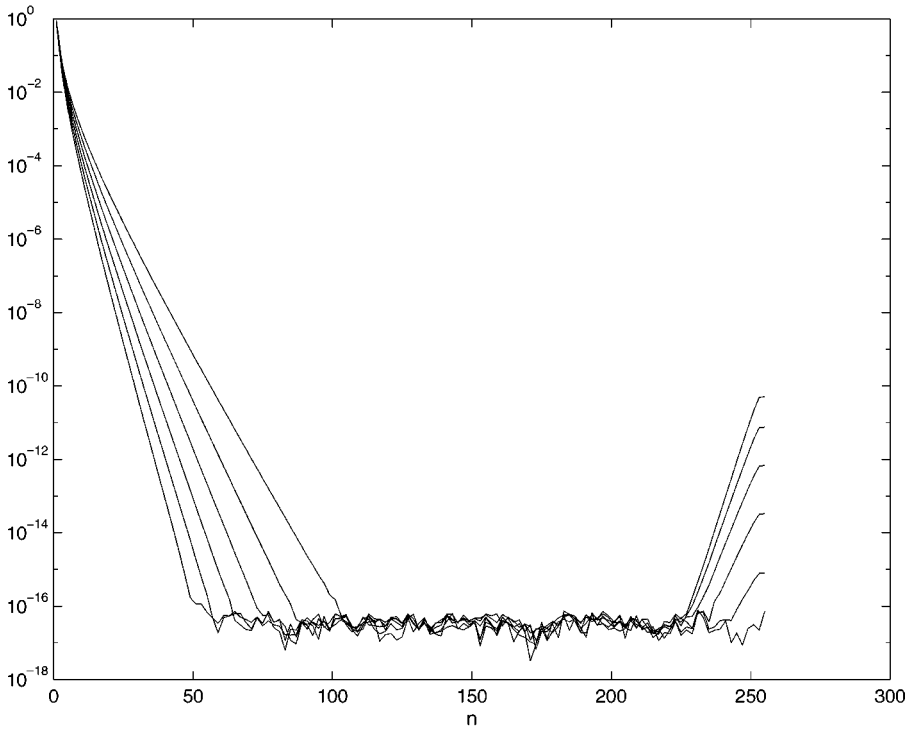

FIG. 2. The Fourier transforms $\log|\hat{\tau}_n|$ of the evolution of an elliptical drop ($\lambda = 1$) with aspect ratio $1/2$ at times 0:(0.2):1, in a nonpadded simulation.

the discrete system to identify the source of this instability and the role played by different spatial discretizations of the velocity. By computing the eigenvalues of the Jacobian matrix corresponding to the right-hand side of (17), we demonstrate numerically that the unpadded computations appear to be unstable, while the padded ones seem stable.

We consider a deformed elliptical drop and compute numerically the Jacobian matrix at this initial state. The plots of the eigenvalues are shown in Fig. 3. As N increases, linear growth of positive, real eigenvalues can be seen in the unpadded computations. These plots have been truncated, we do not show the largest negative eigenvalues, but the magnitude of the eigenvalues increase linearly in N, thus confirming our expectation that a stable time step size will be $O(1/N)$.

We discussed briefly in Section 5.1 an alternative frame of reference for the parametrization, the complexity measuring frame. This frame adaptively clusters marker points in regions of high curvature, the advantage being that fewer modes will be required to fully resolve the interface. Unfortunately, this has an adverse effect on the stability requirements as we see again, by computing the eigenvalues of the Jacobian matrix. Figure 4 shows plots of the full spectrum for the Jacobian matrix. Note that the largest negative eigenvalues are decreasing at such a rate as to suggest a stable time-step size of $O(1/N^2)$. Note also that there is a large gap in the magnitude of the eigenvalues with negative real parts, thus this system is exhibiting stiffness. It may be argued that this stiffness is simply the result of this particular frame, but we know that a large disparity in the magnitude of the eigenvalues was also witnessed in [34]. Here, marker points are updated using a Lagrangian approach and are postprocessed based on equidistributing the curvature of the interface.

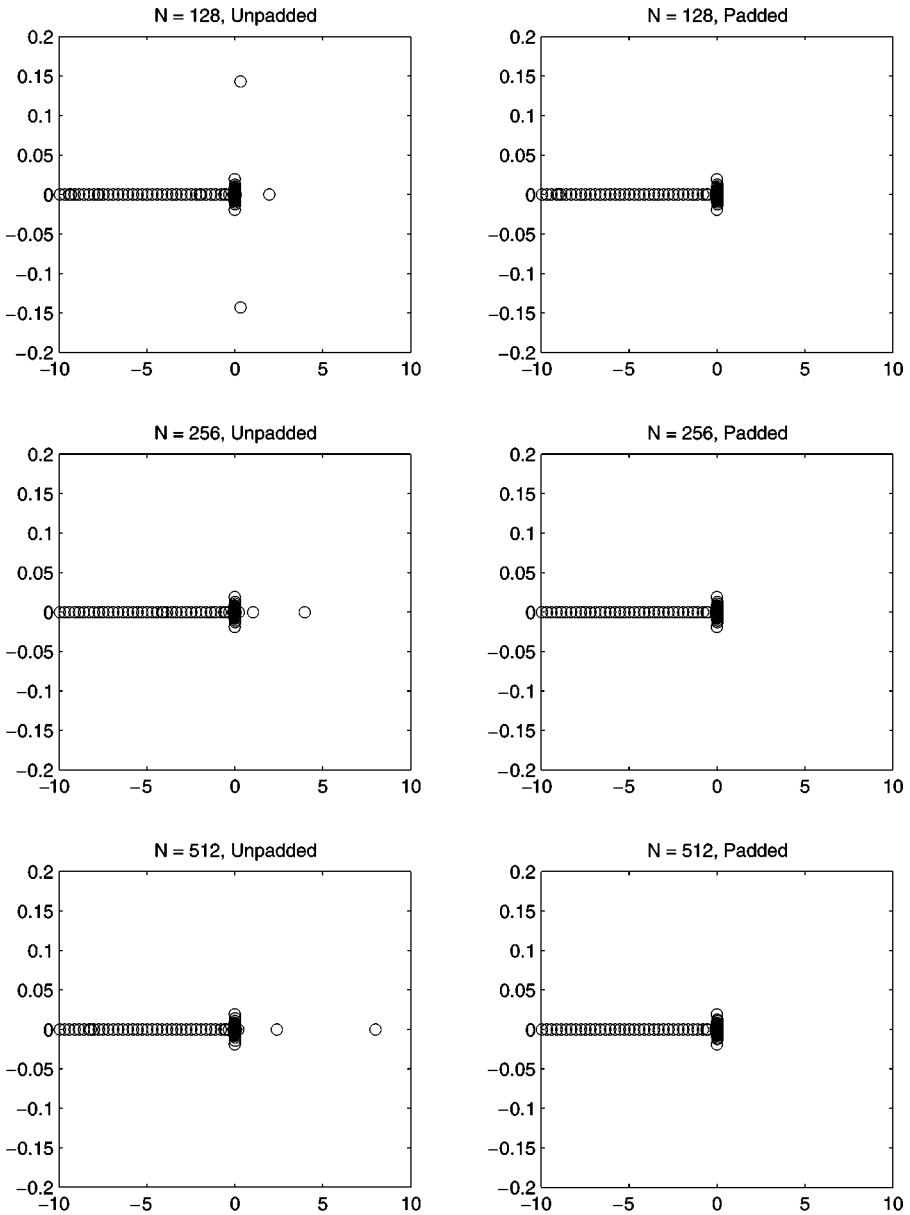

FIG. 3. The instantaneous eigenvalues of the Jacobian matrix of an elliptical drop ($\lambda = 1$) with aspect ratio $4/5$.

EXAMPLE 2: A RELAXING DROP WITH $\lambda = 1$. In this example, we consider the evolution of a deformed viscous drop toward a circular steady state. Here, the viscosity of the drop is the same as that of the ambient fluid, thus the solution to the integral equation is trivial. We use this example to numerically verify that the small-scale decomposition in Section 5.2 accurately describes the nature of the stability constraint on the interface and to compare the performance of the IMEX scheme versus Runge–Kutta.

We consider elliptical profiles with varying aspect ratios, normalized so that their area is π. Figure 5 shows the evolution of a drop with initial aspect ratio of $1/12$. In Fig. 6, we show plots of the Fourier transform for both IMEX and Runge–Kutta at two different

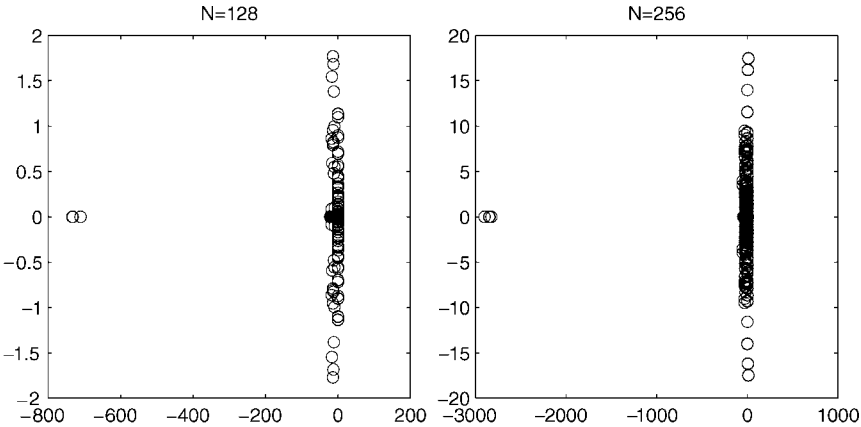

FIG. 4. The instantaneous eigenvalues of the Jacobian matrix of an elliptical drop ($\lambda = 1$) with aspect ratio $4/5$. Complexity Measuring Frame with $C(\kappa) = 1 + \kappa^2$.

time steps. The Runge–Kutta method is unstable at $\Delta t = 0.05$, while the IMEX scheme is clearly stable. Computational information from using the Runge–Kutta method is shown in Table I. Here, Error (A) is the relative error in the cross-sectional area and Error$(s_\alpha) = (\max|z_\alpha| - \min|z_\alpha|)/\max|z_\alpha|)$. We can see from this table that the stable step size varies with $1/N$, as predicted by the analysis in Section 5.2. For comparison, we show computational data for the IMEX scheme in Table II for the evolution of the drop with initial aspect ratio of $1/12$. From this table, we can see that we are able to take very large stable step sizes using the IMEX scheme, but at a significant loss of accuracy.

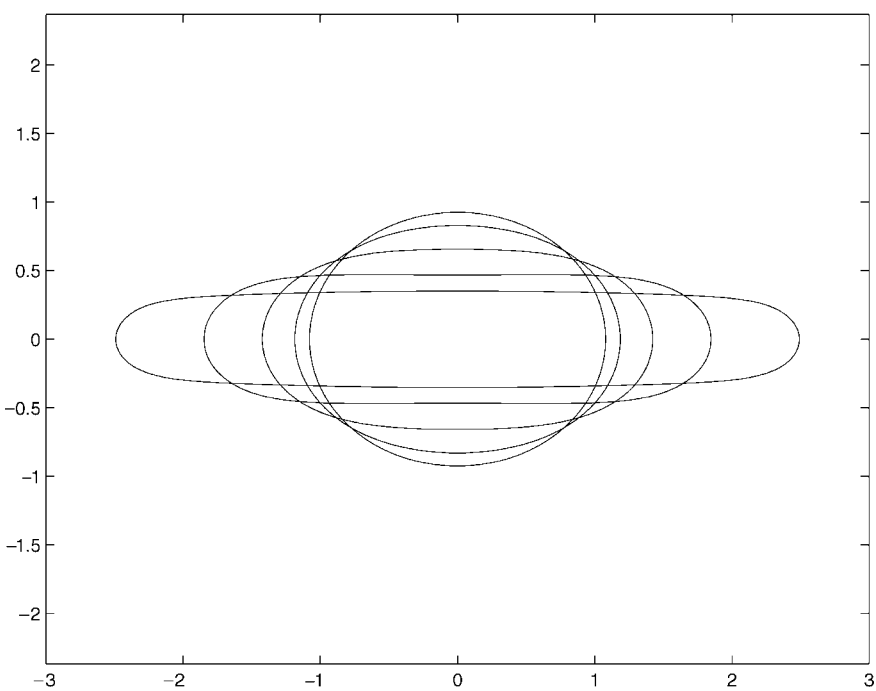

FIG. 5. The evolution of an elliptical viscous drop ($\lambda = 1$) toward a circular steady state; $N = 8192$ and the initial aspect ratio is $1/12$.

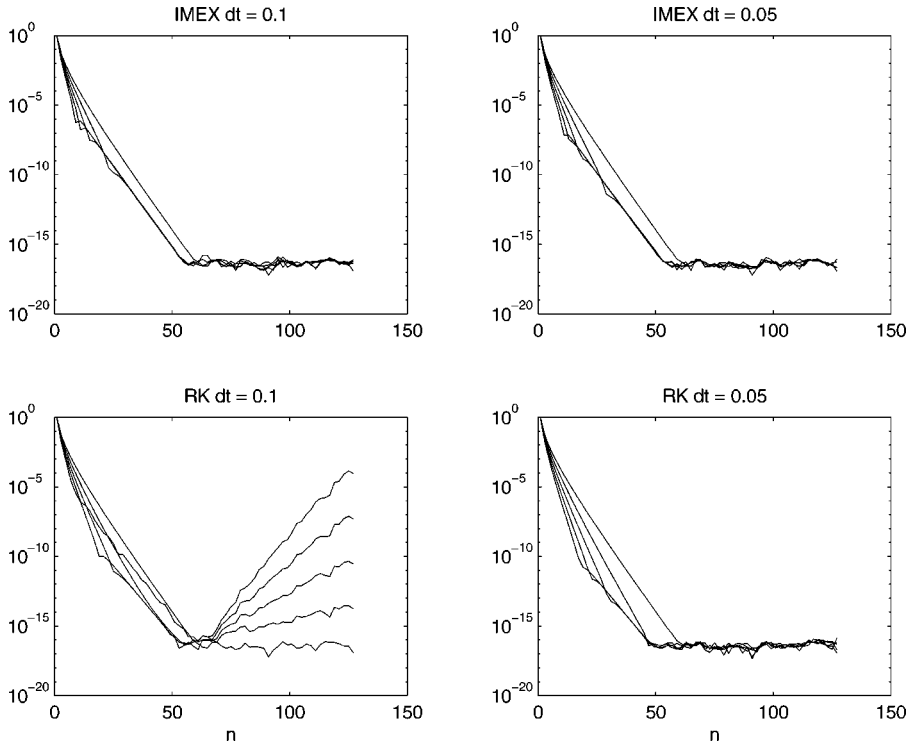

FIG. 6. The Fourier transforms $\log|\hat{\tau}_n|$ of the evolution of the ellipse with aspect ratio $2/3$ at 5 instances in time, for IMEX and Runge–Kutta at two time steps $\Delta t = 0.1$ and $\Delta t = 0.05$.

Since fourth-order IMEX schemes require only an increase in computer memory, not CPU, we experimented with the fourth-order IMEX scheme discussed in [2] in hopes of achieving higher accuracy. Unfortunately, this scheme appears to have a stability requirement similar to the Runge–Kutta method and still does not achieve the same level of accuracy. Thus, we use the Runge–Kutta method for the remaining examples.

EXAMPLE 3: DROP BREAKUP. We now consider the deformation of a drop with $\lambda = 1$ placed in an extensional flow,

$$u_\infty = \mathcal{C}x, \quad v_\infty = -\mathcal{C}y,$$

TABLE I
Computational Information for the Evolution of Elliptical Drops toward Steady State Using Runge–Kutta

Aspect Ratio	N	Δt	t_f	Error (A)	Error (s_α)
2/3	256	0.05	4.0	2.8376×10^{-8}	1.3097×10^{-7}
1/3	512	0.025	4.75	1.2112×10^{-9}	2.0251×10^{-7}
1/6	2048	0.00625	6.275	1.0313×10^{-11}	7.3435×10^{-7}
1/12	8192	0.0015625	8.65625	3.7302×10^{-12}	1.6695×10^{-7}

Note. Δt is the largest stable step size and t_f is the approximate time to steady-state.

TABLE II
IMEX Method for the Evolution of a Drop with Initial Aspect Ratio of 1/12

Δt	Error (A)	Error (s_α)
0.1	1.2249×10^{-3}	3.5133×10^{-1}
0.05	3.1073×10^{-4}	1.2185×10^{-1}
0.025	7.8291×10^{-5}	3.7225×10^{-2}
0.0015625	3.0840×10^{-7}	1.8312×10^{-4}

where $\mathcal{C}$ is the dimensionless capillary number defined by

$$\mathcal{C} = \frac{\gamma \mu a}{\sigma}.$$

In the numerical study [6], Buckmaster and Flaherty computed steady-state drop shapes for various values of $\mathcal{C}$. They demonstrated that for values of the parameter $\Omega = 4\pi\mathcal{C}\sqrt{A}$ less than 4.1, drops in an extensional flow will deform to a steady-state. They were unable to compute steady-state solutions beyond this parameter value and argued that this maximum coincides with the onset of bursting.

An initially circular drop is placed in an extensional flow with $\mathcal{C} = 0.2$ which corresponds to $\Omega = 4.4547$. The deformation of this drop until $t = 50$ is shown in Fig. 7, and the drop's shape at $t = 60$ is shown in Fig. 8. The CPU time required for this simulation was

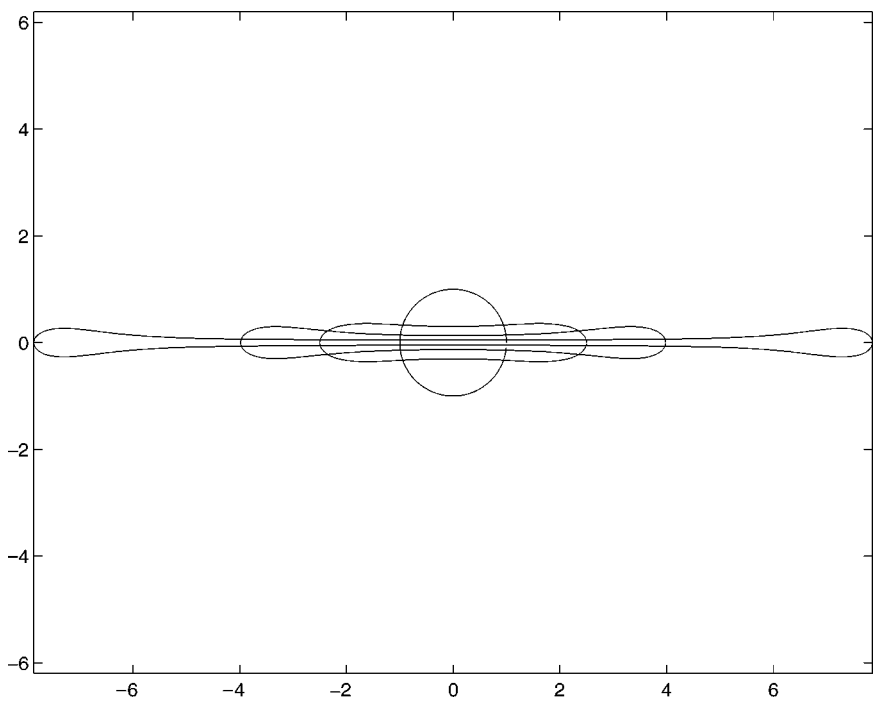

FIG. 7. Deformation of a drop ($\lambda = 1$) in an extensional flow with $\mathcal{C} = 0.2$. This plot shows the evolution from $t = 0$ to $t = 50$. Error (A) $= 6.545 \times 10^{-7}$, Error (s_α) $= 2.6833 \times 10^{-5}$.

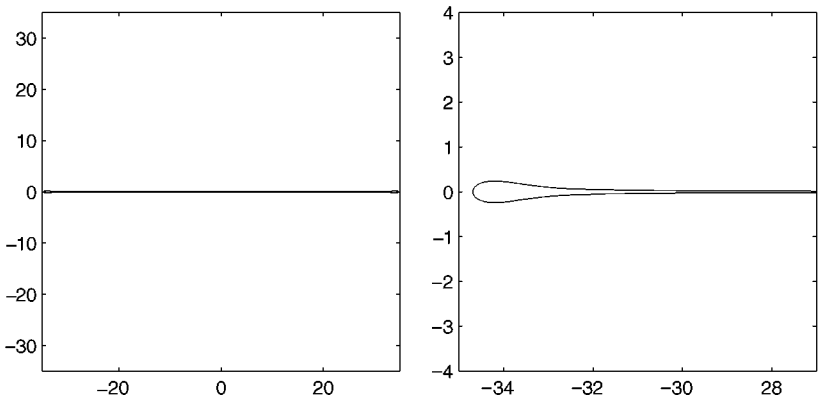

FIG. 8. The profile of a drop at $t = 60$. A close up of the left tip is shown in the plot on the right. Error $(A) = 8.017 \times 10^{-6}$, Error $(s_\alpha) = 1.404 \times 10^{-5}$. The minimum width of the neck is 0.016.

8884 seconds. Clearly, the drop profile is not tending toward a steady-state, confirming the prediction in [6]. Further calculations past pinch-off is the subject of future investigation.

EXAMPLE 4: THE INITIAL COALESCENCE OF TWO EQUAL CIRCLES. In this example, we consider a problem for which there exists both an analytic solution and previous numerical results. We examine a model for the coalescence of two cylindrical drops of fluid just after touching. This is an example for which the fluid domain is bounded by Γ. The evolution of two coalescing cylinders with initial radius $(-R, 0)$ and $(R, 0)$ is described parametrically by [16, 35]

$$x(\alpha', \nu) = \frac{(1-\nu^2)(1-\nu)R\sqrt{2}\cos\alpha'}{(1-2\nu\cos 2\alpha' + \nu^2)\sqrt{1+\nu^2}}$$

$$y(\alpha', \nu) = \frac{(1-\nu^2)(1+\nu)R\sqrt{2}\sin\alpha'}{(1-2\nu\cos 2\alpha' + \nu^2)\sqrt{1+\nu^2}},$$

where ν specifies the degree of coalescence. This parameter has a value of 1 at initial contact, decreases to a value of zero as $t \to \infty$ and evolves according to

$$\frac{d\nu}{dt} = -\frac{\pi R}{\sqrt{2}}\nu\sqrt{1+\nu^2}K(\nu^2), \tag{31}$$

where K is the complete elliptic integral of the first kind defined by

$$K(m) = \int_0^{\pi/2} (1 - m\sin^2\phi)^{-1/2}\, d\phi.$$

In this example, the line of contact is the y-axis and the point on the boundary at the line of contact is refered to as the *neck*. The curvature κ^* at the neck is given by

$$\kappa^* = -\frac{(1-6\nu+\nu^2)\sqrt{1+\nu^2}}{(1-\nu)^3 R\sqrt{2}}.$$

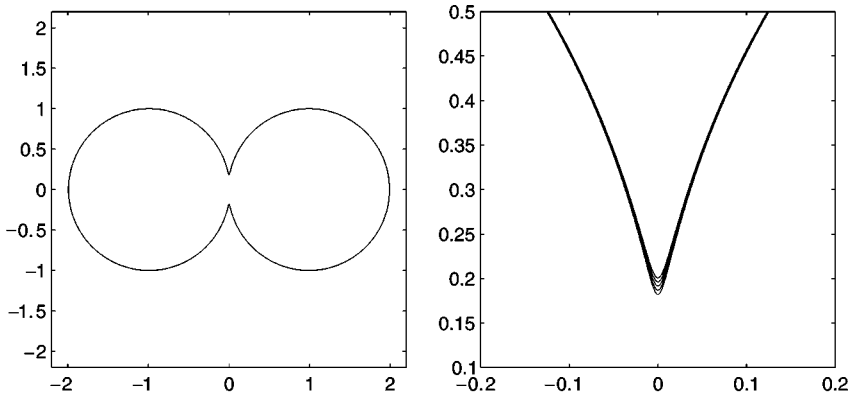

FIG. 9. The left plot shows the initial profile, the curvature at the neck has a value of 700. The right plot shows the early stages of coalescence in the neck region $t = 0{:}(0.004){:}0.02$.

To compare with previously reported numerical results [34, 35], we start with the profile shortly after touching, with a curvature value of 700 at the neck. Figure 9 shows both the initial profile and a blow up of the neck region in the initial stages of coalescence. A large number of points is needed to spectrally resolve the interface, $N = 32768$, and the time step size is $\Delta t = 0.0002$. Figure 10 shows both the evolution of the neck curvature and the error in the computed solution. (The exact curvature was found by integrating (31) using a high-order Runge–Kutta package with the error tolerances set to $<10^{-12}$.) The CPU time needed up to the final time of 0.02 was 25 hours.

The method described in [34, 35] uses a polygonal approximation to the interface, refinement of the mesh in the contact region, and Gaussian elimination for the solution to the integral equation (thus an $O(N^3)$ method). They find their simulations to be stiff and thus employ backward-difference formulae (BDF), with the required Jacobian evaluations, for the implicit treatment of the evolution equations. For this problem, they have appeared to use only 200 points to describe the interface. The effect of this underresolution is clear; the

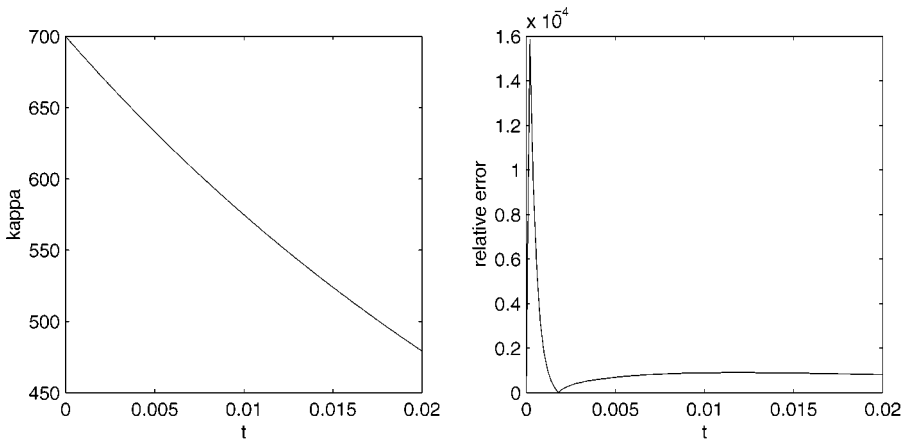

FIG. 10. The left plot shows the evolution of κ^* and the right plot shows the error in the computed solution versus the analytical solution.

error in the computed curvature is nearly 40% during this initial stage. It is interesting to note that our stable explicit time step size is only five times smaller than that used by the BDF scheme.

This example provides an indication of the ability of our methods to handle large-scale problems. Because of the linear scaling of the computational costs of our methods, we could, in approximately the same CPU time, run a simulation of 128 moderately deformed bubbles or drops with $N = 256$ on each for about 10,000 times steps. This would well surpass the larger simulations seen in previously reported works.

EXAMPLE 5: A CONTRACTING BUBBLE IN A QUIESCENT FLOW. In [33], Tanveer and Vasconcelos exploit the complex variable theory for the biharmonic equation to derive analytical solutions for a large class of time-evolving bubbles in a two-dimensional Stokes flow. We use one of their solutions here for comparison.

We consider a bubble placed in a quiescent flow undergoing a contraction rate $\mathring{A} = m$. The bubble shape is described initially by

$$z(\alpha', 0) = a(0)e^{-i\alpha'} + b_N(0)e^{iN\alpha'}, \quad \alpha' \in [0, 2\pi], \tag{32}$$

where $a(0), b_N(0) > 0$. The bubble is symmetrical with respect to the x-axis and has $(N + 1)$-fold symmetry. As argued in [33], the bubble will evolve according to

$$z(\alpha', t) = a(t)e^{-i\alpha'} + b_N(t)e^{iN\alpha'},$$

where the evolution of $a(t)$, $b_N(t)$ and the bubble area $A(t)$ are found through

$$\begin{aligned} \frac{d}{dt}(ab_N) &= -(N+1)ab_N I_0(a, b_N), \\ A(t) \equiv \pi\left[a^2(t) - Nb_N^2(t)\right] &= A(0) + mt. \end{aligned} \tag{33}$$

Here,

$$\begin{aligned} I_0(a, b_N) &= \frac{1}{2\pi}\int_0^{\pi} \frac{d\alpha'}{\left\{a^2 + N^2 b_N^2 - 2Nab_N\cos(\alpha')\right\}^{1/2}} \\ &= \frac{1}{\pi|a|}\frac{\rho}{\rho+1}K\left[\frac{4\rho}{(1+\rho)^2}\right], \end{aligned}$$

where $\rho = a/Nb_N$, and K is the complete elliptic integral of the first kind. (Note: The above corrects an error in [33] for the evaluation of I_0 in terms of K.) See Fig. 11 for the collapse of an initial shape with four-fold symmetry and Table III for computational details. Toward the end of the simulation, the bubble forms near-cusps on the interface, and according to the analysis in [33], the bubble will continue to collapse in a sequence of geometrically similar shapes until all of the air has been removed.

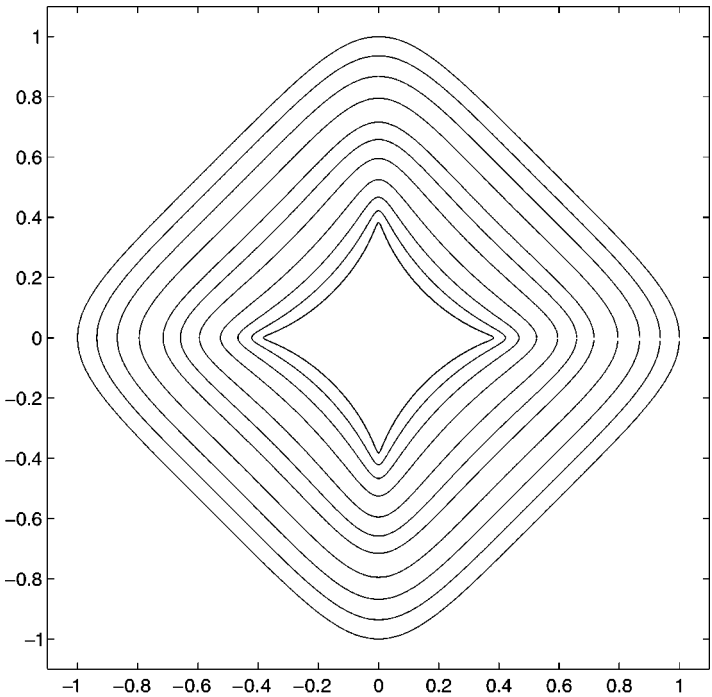

FIG. 11. The evolution of a collapsing four-fold symmetric bubble. The initial shape is given by $a(0) = 0.9$, $b_3(0) = .1$, $A(0) = 0.78\pi$ and the contraction rate is $m = -2\pi$. The final, inner, shape at $t = 0.356$ has $A = 0.2136$ and $\kappa^* = 469$.

The coefficients $a(t)$ and $b_N(t)$ are found by integrating the initial-value problem (33) directly, using a high-order Runge–Kutta package with small error tolerances (tol $< 10^{-10}$). From this solution, we compute the maximum curvature κ^* on the interface from

$$\kappa^*(t) = \frac{a(t) + b_N(t)N^2}{(a(t) - b_N(t)N)^2}.$$

We compare the accuracy of our methods against this maximum curvature. The results are shown in Fig. 12.

Finally, we compute the evolution of collapsing drops of varying viscosity ratios undergoing the same contraction rate as the above example. We attempted to simulate to the same final time $t = 0.356$, although some drops exhibit cusp-formation before that time

TABLE III
Computational Data for the Collapsing Bubble Problem

Δt^0	Error in A	Error in $\lvert z_\alpha \rvert$	*CPU* seconds
0.005	1.2495×10^{-6}	9.1179×10^{-6}	3.636×10^3
0.0025	1.5718×10^{-7}	2.3802×10^{-6}	9.023×10^3
0.00125	1.9710×10^{-8}	6.0794×10^{-7}	1.821×10^4

Note. $N = 512$ on the initial profile and doubles to a value of $N = 8192$. Δt^0 refers to the initial time step.

TABLE IV

Computational Data for Collapsing Drops of Varying Viscosity Ratio

λ	N_f	t_f	κ_f^*	# GMRES Iter/time step
0.1	2048	0.3560	79.1	6–10
0.5	32768	0.3540	225.84	5–11
5.0	32768	0.2967	552.29	5–14
10.0	32768	0.2873	898.92	6–17

Note. $\Delta t^0 = 0.005$ in all cases, and N_f refers to N at the final time step, κ_f^* is the maximum curvature at the final time step.

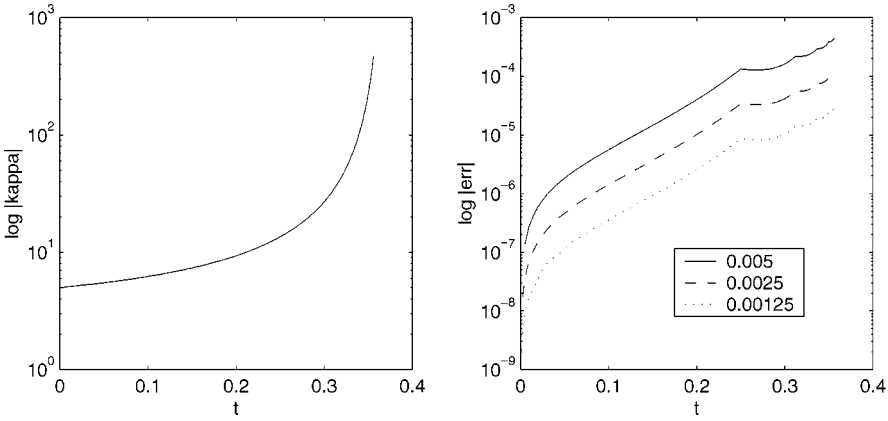

FIG. 12. The left plot shows the evolution of κ^* and the right plot shows the error in the computed solution versus the analytical solution for three different initial time steps. Note: the kinks in the error plots correspond to points when N is doubled.

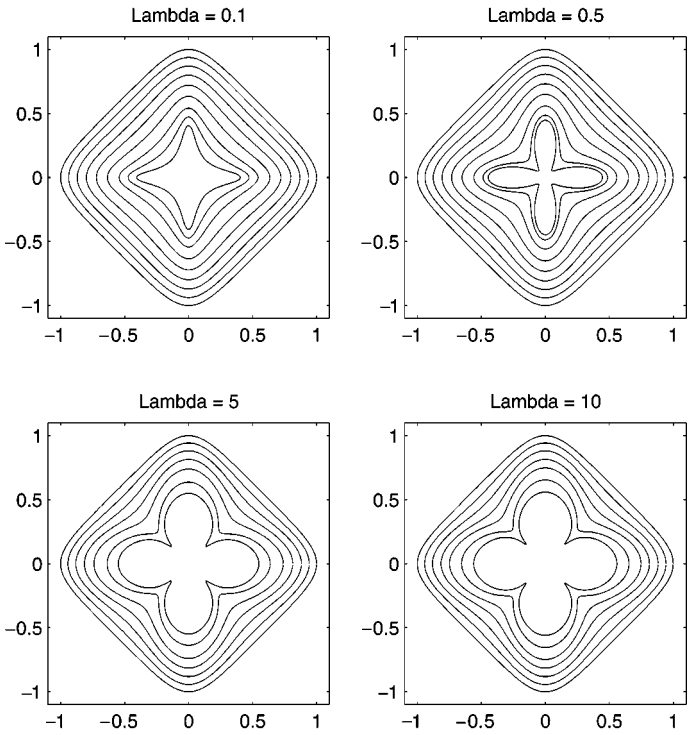

FIG. 13. Collapsing drops of varying viscosity ratios.

and the simulation terminates early. The profiles are shown in Fig. 13 and computational information is shown in Table IV.

8. CONCLUSIONS

In this paper, we present an analysis and new numerical methods for computing the motion of closed fluid interfaces in a Stokes flow. These methods have three important advantages. The first is that they are spectrally accurate. A spectral mesh is used for the description of the interface, and the velocity at the marker points is calculated from the solution to an integral equation using a pseudospectral method. Second, the solution to the integral equation is fast, requiring only $O(N)$ operations, where N is the number of marker points. This makes our methods highly amenable to large-scale simulations. Third, by using evolution equations that preserve equal arclength spacing of the marker points, a low-order stability constraint is maintained. Extensions to multiply-connected domains with inviscid ($\lambda = 0$) closed interfaces are considered in [21]. This work discusses the solution to integral equations similar to the one presented in Appendix A for elasticity problems in multiply-connected domains. Future work will involve developing methods for simulating a large numbers of drop interactions, including the breakup and coalescence phenonema.

APPENDIX: THE SECOND FUNDAMENTAL PROBLEM IN ELASTICITY

The representations for ϕ and ψ in Section 4.1 come directly from those given in [13] to solve the second fundamental problem in elasticity. In this section, we outline this problem and show its equivalence to the boundary-value problem for a fluid interface bounding a domain containing a viscous fluid. To demonstrate the potential for the above methods to be extended to multiply-connected domains, we include the necessary modifications to the representations for the Goursat functions. (Multiply-connected problems in elasticity in the plane and two-dimensional Stokes flow are discussed in detail in [13], and we refer the reader to this work.)

The second fundamental problem in plane elasticity is to find the state of equilibrium of a bounded elastic material when given external stresses are applied to its boundary Γ. Here, we consider Γ to be $(M+1)$-ply connected, with an outer boundary denoted by Γ_0 and the interior contours by $\Gamma_1, \Gamma_2, \ldots, \Gamma_M$. The boundary conditions for this problem in terms of the appropriate Goursat functions are [13]

$$\Phi(\tau) + \tau\overline{\Phi'(\tau)} + \overline{\Psi(\tau)} = g_1(\tau) + ig_2(\tau) + A(k), \quad \tau \in \Gamma_k. \tag{A.1}$$

The left-hand side of (A.1) represents integrated components of stress, and $g_1 + ig_2$ is boundary data obtained from integrated components of applied forces acting on Γ_k. The terms $A(k)$ are constants of integration with $A(0)$ being arbitrarily set to zero.

As suggested by Sherman [25, 26] and outlined in [13], the representations for $\Phi(z)$ and $\Psi(z)$ used to satisfy (A.1) are

$$\Phi(z) = \frac{1}{2\pi i}\int_\Gamma \frac{\rho(\xi)}{\xi - z}\,d\xi,$$

$$\Psi(z) = \frac{1}{2\pi i}\int_\Gamma \frac{\overline{\rho(\xi)}\,d\xi + \rho(\xi)\,d\bar{\xi}}{\xi - z} - \frac{1}{2\pi i}\int_\Gamma \frac{\bar{\xi}\rho(\xi)}{(\xi - z)^2}\,d\xi + \sum_{k=1}^{M}\frac{b_k}{z - z_k}, \tag{A.2}$$

where $\rho(\xi)$ is the unknown complex density, z_k are arbitrary points inside the component curves Γ_k, and the b_k are real constants defined by

$$b_k = i \int_{\Gamma_k} \rho(\xi)\, d\bar{\xi} - \overline{\rho(\xi)}\, d\xi.$$

Letting z tend to a point τ on Γ, we obtain from (A.1) the Sherman–Lauricella integral equation

$$\rho(\tau) + \frac{1}{2\pi i} \int_\Gamma \rho(\xi)\, d \ln \frac{\xi - \tau}{\xi - \bar{\tau}} - \frac{1}{2\pi i} \int_\Gamma \overline{\rho(\xi)}\, d \frac{\xi - \tau}{\xi - \bar{\tau}} + \frac{\bar{B}_0}{\bar{\tau} - \overline{z_*}} + \sum_{k=1}^{M} \frac{b_k}{\bar{\tau} - \overline{z_k}} - A(k) = g(\tau), \tag{A.3}$$

where $g(t) = g_1(t) + i g_2(t)$, $A(0) = 0$, and

$$A(k) = -\int_{\Gamma_k} \rho(\xi)\, ds.$$

Here,

$$B_0 = \frac{1}{2\pi i} \int_\Gamma \left[\frac{\rho(\xi)}{(\xi - z_*)^2}\, d\tau + \frac{\overline{\rho(\xi)}}{(\xi - \overline{z_*})^2}\, d\bar{\xi} \right],$$

and z_* is an arbitrary point in the domain D. As discussed in [13], the addition of source singularities inside each of the component curves completes the rank deficiency of the integral operator in the case of multiply-connected domains.

To establish the equivalence of the stress problem with the interface problem defined by (7) for $\lambda = 0$, identify ϕ with $-i\Phi$, ψ with $-i\Psi$, and $-ig$ with $-(1/2)\tau_s$. Then (7) clearly can be written in the form (A.1). Thus, we obtain the representations for ϕ and ψ in (10) and the integral equation (11) directly from (A.2) and (A.3) with $\omega = -i\rho$ and $M = 0$.

ACKNOWLEDGMENTS

The author thanks the following for many useful suggestions and discussions: Leslie Greengard, Mary Pugh, Bob Russell, Steve Ruuth, and Brian Wetton. She would also like to thank Mike Shelley for pointing out the work by Baker and Nachbin.

REFERENCES

1. L. K. Antanovskii, A plane inviscid incompressible bubble placed within a creeping viscous flow: formation of a cusped bubble, *Eur. J. Mech. B/Fluids* **13**, 491 (1994).
2. U. M. Ascher, S. J. Ruuth, and B. T. R. Wetton, Implicit-explicit methods for time-dependent partial differential equations, *SIAM J. Numer. Anal.* **32**, 797 (1995).
3. U. M. Ascher and L. R. Petzold, *Computer Methods for Ordinary Differential Equations and Differential Algebraic Equations* (Soc. for Industr. & Appl. Mech., Philadelphia, 1998).

4. U. M. Ascher, S. J. Ruuth, and R. J. Spiteri, Implicit-explicit Runge–Kutta methods for time-dependent partial diffential equations, *Appl. Numer. Math.* **25**, 151 (1997).
5. G. Baker and A. Nachbin, Stable methods for vortex sheet motion in the presence of surface tension, *SIAM J. Sci. Comp.* **19**, 1737 (1998).
6. J. D. Buckmaster and J. E. Flaherty, The bursting of two-dimensional drops in slow viscous flow, *J. Fluid Mech.* **60**, 625 (1973).
7. George F. Carrier, Max Krook, and Carl E. Pearson, *Functions of a Complex Variable* (McGraw-Hill, New York, 1966).
8. J. Carrier, L. Greengard, and V. Rokhlin, A fast adaptive multipole algorithm for particle simulations, *SIAM J. Sci. Statist. Comput.* **9**, 669 (1988).
9. R. Charles and C. Pozrikidis, Significance of the dispersed-phase viscosity on the simple shear flow of suspensions of two-dimensional liquid drops, *J. Fluid Mech.* **365**, 205 (1998).
10. Jens Eggers, John R. Lister, and Howard A. Stone, Coalescence of liquid drops, *J. Fluid Mech.* **401**, 292 (1999).
11. A. Greenbaum and A. Mayo, Fast parallel iterative solution of Poisson's and the biharmonic equations on irregular regions, *SIAM J. Sci. Stat. Comp.* **13**, 101 (1992).
12. L. Greengard, *The Rapid Evaluation of Potential Fields in Particle Systems* (MIT Press, Cambridge, MA,1988).
13. L. Greengard, M. Catherine Kropinski, and A. Mayo, Integral equation methods for Stokes flow and isotropic elasticity in the plane, *J. Comput. Phys.* **125**, 403 (1996).
14. L. Greengard and V. Rokhlin, A new version of the fast multipole method for the Laplace equation in three dimensions, *Acta Numerica* **6**, 229 (1997).
15. L. Greengard and V. Rokhlin, Rapid evaluation of potential fields in three dimensions, in *Vortex Methods*, edited by C. Anderson and C. Greengard, Lecture Notes in Mathematics **1360**, (Springer-Verlag, New York, 1998) pp. 121–141.
16. Robert W. Hopper, Plane Stokes flow driven by capillarity on a free surface, *J. Fluid Mech.* **213**, 349 (1990).
17. Hua Zhou and C. Pozrikidis, The flow of suspensions in channels: Single files of drops, *Phys. Fluids A* **5**, 311 (1993).
18. Thomas Y. Hou, John S. Lowengrub, and Michael J. Shelley, Removing the stiffness from interfacial flows with surface tension, *J. Comput. Phys.* **114**, 312 (1994).
19. M. A. Jaswon and G. T. Symm, *Integral Equation Methods in Potential Theory and Elastostatics* (Academic Press, New York, 1977).
20. M. C. A. Kropinski, Integral Equation Methods for Particle Simulations in Creeping Flows, *Computers Math. Appl.* **38**, 67 (1999).
21. M. C. A. Kropinski, Numerical methods for multiple inviscid interfaces in creeping flows, submitted for publication.
22. W. E. Langlois, *Slow Viscous Flow* (Macmillan Co., New York, 1964).
23. M. R. Kennedy, C. Pozrikidis, and R. Skalak, Motion and deformation of liquid drops, and the rheology of dilute emulsions in simple shear flow, *Comput. Fluids* **23**, 251 (1994).
24. S. G. Mikhlin, *Integral Equations* (Pergammon Press, London, 1957).
25. S. G. Muskhelishvili, *Some Basic Problems of the Mathematical Theory of Elasticity* (Noordhoff, Groningen, 1953).
26. V. Z. Parton and P. I. Perlin, *Integral Equation Methods in Elasticity* (Mir, Moscow, 1982).
27. C. Pozrikidis, Numerical studies of singularity formation at free surfaces and fluid interfaces in two-dimensional Stokes flow, *J. Fluid Mech.* **331**, 145 (1997).
28. S. Richardson, Two-dimensional bubbles in slow viscous flows, *J. Fluid Mech.* **33**, 476 (1968).
29. V. Rokhlin, Rapid solution of integral equations of classical potential theory *J. Comput. Phys.* **60**, 187 (1985).
30. Y. Saad and M. H. Schultz, GMRES: a generalized minimum residual algorithm for solving nonsymmetric linear systems, *SIAM J. Sci. Stat. Comput.* **7**, 856 (1986).
31. Michael J. Shelley and Tetsuji Ueda, The Stokesian hydrodynamics of flexing, stretching filaments, submitted for publication.

32. I. S. Sokolnikoff, *Mathematical Theory of Elasticity*, (McGraw-Hill, New York, 1956).
33. Saleh Tanveer and Giovani L. Vasconcelos, Time-evolving bubbles in two-dimensional Stokes flow, *J. Fluid Mech.* **301**, 325 (1995).
34. G. A. L. van de Vorst and R. M. M. Mattheij, A BEM- BDF scheme for curvature driven moving Stokes flows, *J. Comput. Phys.* **120**, 1 (1995).
35. G. A. L. van de Vorst and R. M. M. Mattheij, Numerical Analysis of a 2-D viscous sintering problem with non-smooth boundaries, *Computing* **49**, 239 (1992).
36. A. Z. Zinchenko, M. A. Rother, and R. H. Davis, Cusping, capture and breakup of interacting drops by a curvatureless boundary-integral algorithm, *J. Fluid Mech.* **391**, 249 (1999).